Phase diagram and quantum transport in a semiconductor-superconductor hybrid nanowire with long-range pairing interactions

Jun-Tong Ren,[1] Sha-Sha Ke,[1] Yong Guo,[2] Huai-Wu Zhang,[1] and Hai-Feng Lü[1,2,*]

[1]*School of Physics and State Key Laboratory of Electronic Thin Films and Integrated Devices, University of Electronic Science and Technology of China, Chengdu 610054, China*

[2]*Department of Physics and State Key Laboratory of Low-Dimensional Quantum Physics, Tsinghua University, Beijing 100084, China*

(Received 26 July 2020; revised 13 November 2020; accepted 6 January 2021; published 28 January 2021)

We investigate the effect of long-range pairing interactions on the phase diagram and the quantum transport properties in a semiconductor-superconductor hybrid nanowire. Both the power-law and exponential decay rates of long-range pairing are considered for comparison. It is found that a long-range topological phase hosting massive edge modes is induced when the exponent of the power-law decay is less than one. By diagonalizing the tight-binding model, we find that near-zero-energy Andreev bound states (ABSs) could be induced in the topologically trivial phase for slowly decayed long-range pairing interactions. For a one-dimensional long-range Kitaev chain, the shot noise is suggested to serve as a probe to discriminate Majorana bound states (MBSs) and topological massive modes. Our numerical results indicate that for realistic device parameters, the Fano factor of the shot noise is irrelevant to the topological property of the system, and it fails to distinguish the MBSs and ABSs. However, the noise Fano factor is generally consistent with the variation of the bound state energy, which can be used to detect the energy splitting of these bound states.

DOI: 10.1103/PhysRevB.103.045428

I. INTRODUCTION

A Majorana fermion is an exotic particle that is its own antiparticle. In recent years, much interest has been drawn to looking for Majorana bound states (MBSs) hosted in topological superconductors. Spatially separated MBSs pairs are promising candidates for the realization of stable qubits in fault-tolerant topological quantum computing [1–5]. The Kitaev chain is the most well-known prototypical model of a one-dimensional topological superconductor [6]. This model is equivalent to the one-dimensional Ising model in a transverse magnetic field, and they can be mapped to each other by performing the Jordan-Wigner transformation. There are two gapped phases for the Kitaev chain, a topologically trivial and a topologically nontrivial phase. A phase transition occurs at the critical point where the mass gap closes. For a topologically nontrivial phase, its main point of interest is that two unpaired real fermionic Majorana modes appear at the end points of the chain.

To explore possible additional novel phases, the study of the Kitaev chain is extended to the case of long-range pairing, hopping, as well as to higher-dimensional cases [7–24]. For a Kitaev chain with long-range pairing, the pairing between sites i and j decays as a power-law function $\Delta_{ij} = \Delta_0 |i - j|^{-\beta}$, where Δ_0 represents the pairing strength between the nearest-neighboring sites and β measures the decay rate of the pairing strength. The phases of the Kitaev chain hosting MBSs appear for $\beta > 1$ and are labeled as short-range pairing. For $\beta < 1$, two new phases with noninteger winding numbers appear. In long-range topological phases, there exist subgap massive modes localized at the chain ends [7]. Different from where Majorana modes are well separated in the infinite chain limit, the wave-function overlap of the massive end modes for $\beta < 1$ always remains finite. How to discriminate these two end modes thus becomes an important task. When the Kitaev chain with long-range pairing is connected to two normal leads, the transport property is expected to disclose the phase signal. The noise Fano factor is suggested to probe the quantum phase transition between the short-range topological phase and the long-range topological phase [25]. Specifically, the Fano factor F is zero in the short-range correlated phase, while $F = 1$ in the long-range correlated phase.

Experimentally, the most promising candidate to realize MBSs is based on conventional s-wave superconductors exposed to strong magnetic fields and proximity coupled to a nanowire with a spin-orbit interaction [26–32]. In the high magnetic field limit, the spin-orbit-coupled nanowire in proximity with s-wave superconductors resembles the Kitaev chain model [33]. These devices provided experimental signatures of MBSs in the form of zero-bias conductance peaks [34–40]. The most recent relevant development has been the observation of a $2e^2/h$ zero-bias quantized conductance plateau [41]. Although the quantized zero-bias conductance peak has been almost universally accepted as the decisive signature satisfying the existence of MBSs, there is no compelling evidence to rule out the effect of partially separated Andreev bound states (ABSs) [42–48]. At this stage, distinguishing MBSs from the trivial ABSs is one of the most urgent goals in Majorana research [49,50].

In most previous studies, the proximity-induced superconducting pairing potential along the nanowire is assumed to

*lvhf04@uestc.edu.cn

be approximately equal and only on-site pairing is taken into account. Recently, long-range pairing and hopping interactions induced by proximity effects have been investigated in the semiconductor-superconductor heterostructure [51–57]. It is found that the induced pairing strength is much smaller than that of the host superconductor [35,36]. The topological phase diagram is thus considerably modified by long-range interactions. However, it remains unknown how the quantum transport properties are affected by long-range pairing interactions.

In this paper, we investigate the effect of long-range pairing interactions on the topological phase diagrams and quantum transport properties in a semiconductor-superconductor hybrid nanowire. General expressions for the winding numbers and the formulae about the current and the shot noise are derived. We separately consider two types of decay rates of the long-range pairing deformation and show their distinction in a phase diagram. The Fano factor of the shot noise is also discussed when the long-range nanowire is connected to two metallic leads. In realistic device parameters, we find that although the noise Fano factor is irrelevant to the topological property of the system, it could serve as a good probe to detect the energy splitting of the bound states.

The paper is organized as follows. In Sec. II we introduce the model Hamiltonian for a nanowire system with long-range pairing terms. The formulae about the winding number and the transport are presented. In Sec. III we discuss the effect of long-range pairing on the phase diagrams of the system. For comparison, we also use the exact diagonalization method to obtain the low-energy spectra for a lattice model. In Sec. IV, we present the numerical results of the Fano factor of the zero-frequency shot noise in both topologically nontrivial and trivial phases. Finally, a summary is given in Sec. V.

II. MODEL AND FORMALISM

A. Theoretical model

We consider a semiconducting nanowire partially covered with an epitaxial superconductor shell in contact with two normal leads. Part of the nanowire is in a superconducting state with long-range pairing interactions induced by the proximity effect. A schematic representation of the setup is illustrated in Fig. 1. The Hamiltonian describing the system has the following form,

$$H = H_L + H_T + H_{\rm NW} + H_\Delta. \tag{1}$$

Here, H_L describes the normal metallic leads and H_T represents the couplings between the nanowire and the leads. $H_{\rm NW}$ is the Hamiltonian of a strongly spin-orbit-coupled nanowire in the presence of a parallel magnetic field. It can be written in a more compact form by introducing the Hamiltonian density $\mathcal{H}_{\rm NW}$,

$$H_{\rm NW} = \frac{1}{2}\int dx \psi^\dagger(x)\mathcal{H}_{\rm NW}\psi(x), \tag{2}$$

$$\mathcal{H}_{\rm NW} = \left(-\frac{\hbar^2}{2m}\partial_x^2 - \mu\right) - i\alpha\partial_x\sigma_y + V_Z\sigma_x, \tag{3}$$

where $\psi(x) = [\Psi_\uparrow(x), \Psi_\downarrow(x)]^{\rm T}$ is the annihilation operator of an electron at position x, m is the effective electron mass, μ represents the chemical potential in the wire, α is the Rashba parameter, and $V_Z = g_{\rm eff}\mu_B B/2$ gives the Zeeman splitting induced by the magnetic field B with $g_{\rm eff}$ the effective g factor and μ_B the Bohr magneton. The Pauli matrices σ_i with $i = x, y, z$ act on the spin degree of freedom.

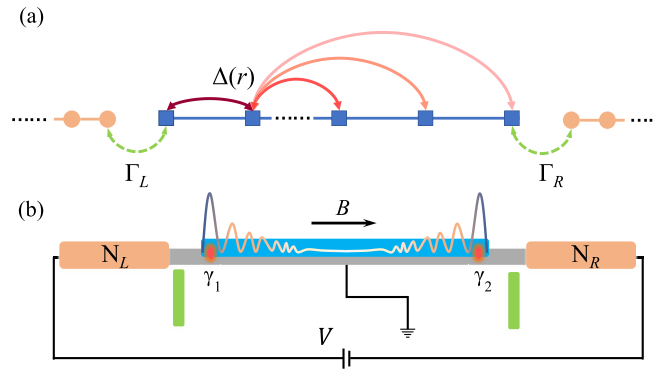

FIG. 1. (a) The long-range superconducting nanowire is in the middle (blue lines and squares). It is in contact with two normal metallic leads (orange lines and disks) through tunnel couplings described by Γ_L and Γ_R. Each site of the nanowire is coupled with every other site by a pairing amplitude $\Delta(r)$. (b) Schematic diagram of the transport setup: A grounded spin-orbit-coupled semiconductor nanowire coated with an epitaxial superconducting shell in a parallel magnetic field B is connected to two normal metallic leads N_L and N_R. A pair of MBSs (γ_1, γ_2) appear at both ends of the covered nanowire segment when the system is in the topological phase. A bias voltage V is applied across the whole device.

The last term H_Δ in Eq. (1) is the proximity-induced s-wave BCS Hamiltonian that couples states with opposite momenta and spins in the nanowire. The specific form of H_Δ depends on various details of the system and on the degree of complexity that we want to incorporate into the model, but here we assume that the superconducting pairing interaction between two electrons depends only on their spatial distance, which takes the generic form

$$H_\Delta = \frac{1}{2}\int dx dx' [\Psi_\uparrow^\dagger(x)\Delta_{|x-x'|}\Psi_\downarrow(x') + \text{H.c.}]. \tag{4}$$

Taking into account the long-range pairing terms originating from the proximity effect, the N-site tight-binding Hamiltonian for the hybrid semiconductor-superconductor nanowire reads [58]

$$H_{\rm TB} = H_0 + H_\Delta, \tag{5}$$

$$H_0 = \sum_{j=1}^{N}[(2t-\mu)c_j^\dagger c_j + V_Z c_j^\dagger \sigma_x c_j] + \sum_{j=1}^{N-1}[-tc_j^\dagger c_{j+1} - it_{\rm SO}c_j^\dagger\sigma_y c_{j+1} + \text{H.c.}], \tag{6}$$

where H_0 discretizes the continuum Hamiltonian of the nanowire, $c_{i,\sigma}$ ($c_{i,\sigma}^\dagger$) annihilates (creates) an electron with spin $\sigma = \uparrow, \downarrow$ on lattice site i, $t = \hbar^2/2ma^2$ represents the nearest-neighbor hopping amplitude, $t_{\rm SO} = \alpha/2a$ describes the spin-orbit coupling, and a is the lattice spacing. The spin indices have been suppressed for brevity. The long-range

pairing terms in the lattice model are given by

$$H_\Delta = \sum_{j,r} \Delta(r) c^\dagger_{j,\uparrow} c^\dagger_{j+r,\downarrow} + \text{H.c.} \tag{7}$$

In the following discussions, we focus on two specific forms of $\Delta(r)$,

$$\Delta_a(r) = \frac{\Delta_0}{(r+1)^\beta}, \tag{8}$$

$$\Delta_b(\ell) = \frac{\Delta_0}{k_F \ell} e^{-\ell/\xi} \sin k_F \ell, \tag{9}$$

where $\ell = ra$ gives the spatial distance between two sites, Δ_0 is the on-site superconducting pairing potential, k_F is the Fermi momentum in the nanowire, and ξ characterizes the coherence length in the host superconductor. Here, Δ_a specifies the long-range pairing interactions that decay as a power-law function of distance with exponent β. This power-law dependence of the long-range interactions has been intensively investigated in recent literature on Kitaev chains with extended hopping and pairing terms, which has been proposed as models for the helical Shiba chains consisting of magnetic impurities on an s-wave superconductor [59]. In particular, the long-range pairing terms for helical Shiba states can be derived explicitly from the effective action of an adatom system weakly coupled to an s-wave superconductor [53], here denoted by Δ_b. This type of long-range pairing exhibits more subtle behavior. It decays slowly as $\sim 1/\ell$ except for a sinusoidal modulation when $\ell \ll \xi$, while for $\ell \gg \xi$ it crosses over into an exponential decay [60].

B. Topological invariant

We proceed to outline the calculation of the topological invariants for a nanowire with long-range pairing terms given in Eqs. (8) and (9). The real-space tight-binding Hamiltonian H_{TB} of Eq. (5) can be transformed into the Bogoliubov–de Gennes (BdG) Hamiltonian in momentum space,

$$\begin{aligned}\mathcal{H}(k) = &-(2t\cos k - \epsilon + 2t_{\text{SO}} \sin k \sigma_y)\tau_z \\ &+ V_Z \sigma_x + \widetilde{\Delta}(k)\tau_x,\end{aligned} \tag{10}$$

with the Nambu representation $[c_{k\uparrow}, c_{k\downarrow}, c^\dagger_{-k\downarrow}, -c^\dagger_{-k\uparrow}]^{\text{T}}$. Here, $\epsilon = 2t - \mu$ is the on-site energy. The Fourier transformed long-range pairing terms with power-law and exponential decaying are given, respectively, as

$$\widetilde{\Delta}_a(k) = \Delta_0 \left[1 + \sum_{r=1}^{\infty} \frac{2\cos kr}{(r+1)^\beta} \right], \tag{11}$$

$$\widetilde{\Delta}_b(k) = \Delta_0 \left[1 + \sum_{r=1}^{\infty} \frac{2\cos kr}{k_F r} e^{-r/\xi} \sin(k_F r) \right]. \tag{12}$$

The one-dimensional system described by $\mathcal{H}(k)$ in Eq. (10) belongs to the class BDI with a $\mathbb{Z}$ invariant in the Altland-Zirnbauer symmetry classification [61,62]. The particle-hole symmetry $\Xi = \tau_y \sigma_y \mathcal{K}$ is respected in the presence of long-range pairing terms, where $\mathcal{K}$ stands for complex conjugation. The BdG Hamiltonian $\mathcal{H}(k)$ can be transformed into a block off-diagonal form by a unitary transformation U as

$$\mathcal{H}'(k) = U\mathcal{H}(k)U^\dagger = \begin{bmatrix} 0 & \mathcal{A}(k) \\ \mathcal{A}(k)^\dagger & 0 \end{bmatrix}, \tag{13}$$

where the determinant of the antidiagonal block $\det \mathcal{A}(k)$ characterizes the eigenenergies of the system. It is given by

$$\mathcal{A}(k) = [\widetilde{\Delta}(k) + 2i t_{\text{SO}} \sin k] - i(2t\cos k - \epsilon)\sigma_y - V_Z \sigma_z. \tag{14}$$

For our one-dimensional system, the Berry connection can be expressed as [61]

$$A_k = \frac{1}{2i} \partial_k \ln(\det \mathcal{A}). \tag{15}$$

The winding number is given by the quantized Berry phase in terms of π over the first Brillouin zone [53],

$$W = \frac{1}{\pi} \oint dk A_k = \frac{1}{2\pi i} \oint dk \partial_k \ln(\det \mathcal{A}). \tag{16}$$

We now define $Z(k) \equiv \det \mathcal{A}$ for compact presentation. It takes the explicit form as

$$Z(k) = (2t\cos k - \epsilon)^2 - V_Z^2 + [\widetilde{\Delta}(k) + 2i t_{\text{SO}} \sin k]^2.$$

We then decompose $Z(k)$ into its polar form and let $\varphi(k) \equiv \arg Z(k)$, and the winding number can be expressed as

$$W = \frac{1}{2\pi i} \oint dk \partial_k [\ln |Z(k)| + i\varphi(k)] = \frac{1}{2\pi} \oint dk \partial_k \varphi(k), \tag{17}$$

where the first term vanishes under closed integration since $|Z(k)|$ is periodic in the first Brillouin zone. Considering that $Z(k)$ is particle-hole symmetric, we have that the equation $-\varphi(k) = \varphi(-k) \mod 2\pi$ holds. Finally, we obtain

$$\begin{aligned} W &= \frac{1}{2\pi} \left[\int_{-\pi}^{0} dk \partial_k \varphi(k) + \int_{0}^{\pi} dk \partial_k \varphi(k) \right] \\ &= \frac{1}{\pi} \int_0^\pi dk \partial_k \varphi(k) \\ &= \frac{1}{\pi} [\varphi(\pi) - \varphi(0)], \end{aligned} \tag{18}$$

which is equivalent to another form [53],

$$W = \tfrac{1}{2} [\text{sgn}\, Z(\pi) - \text{sgn}\, Z(0)]. \tag{19}$$

However, the winding number expression (19) is only applicable for the exponentially decayed pairing $\widetilde{\Delta}_b(k)$ and the power-law decay rate $\widetilde{\Delta}_a(k)$ for $\beta > 1$. For $\beta \leqslant 1$, $\widetilde{\Delta}_a(k)$ becomes divergent at the point $k = 0$, and the topological singularity at this point makes the winding vector ill defined [10]. In this case, band touching is only possible at $k = \pi$ and the winding number has a contribution only from the point $k = \pi$ [63].

In the case of $\beta \leqslant 1$, the real part of $Z(k)$ is only zero for $k = \pi$, leaving the lines $\mu = 4t \pm \sqrt{V_Z^2 - \widetilde{\Delta}_a^2(\pi)}$ gapped. At point $k = 0$, the real part of $Z(k)$ and the dispersion diverge, where the lines $\mu = \pm\sqrt{V_Z^2 - \widetilde{\Delta}_a^2(0)}$ become gapless. Consequently, in the case of a Majorana nanowire with power-law decaying long-range pairings, there are only two different

sectors in the phase diagram below the line $\beta = 1$. To determine the winding number in this case, we note that W has a contribution only from the point $k = \pi$. By linearizing the real and imaginary parts of $Z(k)$ at the point $k = \pi$, it can be deduced that

$$\mathrm{Re}[Z(k)] \sim (4t - \mu)^2 - V_Z^2 + \Delta_0^2[1 - (2 - 2^{2-\beta})\zeta(\beta)]^2,$$
$$\mathrm{Im}[Z(k)] \sim 4t_{\mathrm{SO}}\Delta_0[1 - (2 - 2^{2-\beta})\zeta(\beta)](k - \pi),$$

where $\zeta(\beta)$ is the Riemann zeta function, and the winding number for the case of $\beta \leqslant 1$ can then be given by [63]

$$W = \frac{1}{2\pi}\int_{-\infty}^{\infty} dk\partial_k\varphi(k) = \begin{cases} -\frac{1}{2}, & \text{for } |\mu - 4t| < \sqrt{V_Z^2 - \widetilde{\Delta}_a^2(\pi)}, \\ +\frac{1}{2}, & \text{for } |\mu - 4t| > \sqrt{V_Z^2 - \widetilde{\Delta}_a^2(\pi)}. \end{cases} \quad (20)$$

C. Transport properties via nonequilibrium Green's function method

To demonstrate how the transport properties are modified by long-range pairing terms, we employ the nonequilibrium Green's function (NEGF) method. Following the Keldysh formalism, the retarded Green's function of the system in the Nambu-spinor representation can be calculated by

$$G^r = \left(\epsilon - H_{\mathrm{NW}} - \Sigma_L^r - \Sigma_R^r\right)^{-1}. \quad (21)$$

In the wideband limit, the retarded self-energy due to the γ lead is given by $\Sigma_\gamma^r = -i\hat{\Gamma}_\gamma/2$ and $\hat{\Gamma}_\gamma$ describes the coupling between the wire and the γ lead, which takes the form

$$\hat{\Gamma}_L = \Gamma_L \mathrm{diag}(\hat{1}, \hat{0}, \hat{0}, \ldots, \hat{0})_N, \quad (22)$$

$$\hat{\Gamma}_R = \Gamma_R \mathrm{diag}(\hat{0}, \hat{0}, \hat{0} \ldots, \hat{1})_N, \quad (23)$$

where $\hat{1}$ and $\hat{0}$ are the 4×4 identity and zero matrices. The energy-independent lead-wire couplings are denoted by $\Gamma_\gamma = 2\pi\rho_\gamma|t_\gamma|^2$ with ρ_γ the density of states of the γ lead and t_γ the coupling constant [64]. The lesser self-energies that characterize the particle injection from the leads are given by

$$\Sigma_L^< = \mathrm{diag}(\hat{\Sigma}_L^<, \hat{0}, \hat{0}, \ldots, \hat{0})_N, \quad (24)$$

$$\Sigma_R^< = \mathrm{diag}(\hat{0}, \hat{0}, \hat{0}, \ldots, \hat{\Sigma}_R^<)_N. \quad (25)$$

The nonzero entry $\hat{\Sigma}_\gamma^<$ reads

$$\hat{\Sigma}_\gamma^< = i\Gamma_\gamma \mathrm{diag}\left(f_\gamma^e, f_\gamma^e, f_\gamma^h, f_\gamma^h\right). \quad (26)$$

Here, $f_\gamma^{e(h)}(\omega) = 1/(1 + e^{(\omega \mp \mu_\gamma)/k_BT})$ is the Fermi-Dirac distribution function of the electrons (holes) in the γ lead, and $\mu_{L(R)} = \pm eV/2$ is the chemical potential for the left (right) lead under an applied bias V.

Once the Green's functions and self-energies are obtained, the current flowing from the γ lead into the wire can be formulated as

$$I_\gamma = \frac{e}{h}\int d\omega\left[T_D\left(f_\gamma^e - f_{\bar{\gamma}}^e\right) + T_A\left(f_\gamma^e - f_\gamma^h\right) + T_{CA}\left(f_\gamma^e - f_{\bar{\gamma}}^h\right)\right], \quad (27)$$

where $\gamma = L, R$ and $\bar{\gamma} = R, L$. Here, $T_D = \mathrm{Tr}[\hat{\Gamma}_\gamma^e G^r \hat{\Gamma}_{\bar{\gamma}}^e G^a]$, $T_A = \mathrm{Tr}[\hat{\Gamma}_\gamma^e G^r \hat{\Gamma}_\gamma^h G^a]$, and $T_{CA} = \mathrm{Tr}[\hat{\Gamma}_\gamma^e G^r \hat{\Gamma}_{\bar{\gamma}}^h G^a]$ are the transmission functions contributed by the direct transmission process, the local Andreev reflection, and the crossed Andreev reflection, respectively. The trace is taken over the Nambu-spin space. $G^a = (G^r)^\dagger$ is the advanced Green's function, and $\hat{\Gamma}_\gamma^{e(h)}$ are $4N \times 4N$ matrices that keep only the electron (hole) contributions of Eqs. (22) and (23). More additional details of the derivation on the current are included in the Appendix.

The differential tunneling conductance can then be calculated by $G = dI_\gamma/dV$ and the shot noise can be derived from the Fourier transformed current-current correlation function [65–67]

$$S_{\gamma\gamma'}(\omega) = \int dt e^{i\omega(t-t')}\langle\{\delta\hat{I}_\gamma(t), \delta\hat{I}_{\gamma'}(t')\}\rangle, \quad (28)$$

where $\delta\hat{I}_\gamma(t) = \hat{I}_\gamma(t) - I_\gamma(t)$. The Fano factor of the shot noise is defined as $\mathcal{F} = S/2eI$ with $S = 2S_{LL}(\omega \to 0)$ to measure the deviation from the uncorrelated Poissonian noise for which $F = 1$. The noise Fano factor can be enhanced or suppressed because the current fluctuations in the device are highly susceptible to different interactions in the system.

Throughout this work we set the lattice constant $a =$ 10 nm and restrict our discussion to the zero-temperature limit. A small applied voltage $eV < \Delta$ is taken to ensure that only the near-zero-energy MBSs and the trivial ABSs of the total quasiparticles in the superconductor are important. In the absence of near-zero-energy bound states, the transmission of Cooper pairs through the device is dominated and the noise Fano factor at a low-bias voltage approaches 2 [68].

III. PHASE DIAGRAMS

We first consider the effect of the long-range pairing interaction with a power-law decay rate on the phase diagram of a nanowire system. Different quantum phases could be tuned by varying the chemical potential, Zeeman splitting energy, or the decay rate that characterizes the long-range pairing. The effect of long-range pairing on the phase diagram is illustrated in Fig. 2 as functions of the Zeeman field V_Z and on-site energy ϵ. For the limit $\beta \to \infty$, the long-range pairing interaction is not considered and the system is mapped to an ordinary Majorana nanowire. In this case, the threshold Zeeman field that supports the existence of MBSs is determined by $V_Z^C = \sqrt{\mu^2 + \Delta_0^2}$. The topological phases show a mirror symmetry with respect to the zero on-site energy, while with opposite winding numbers $W = -1$ and $W = +1$.

When modulating β to a finite value, the long-range pairing interactions between different sites are gradually turned on. The symmetry of the phase diagram about the zero on-site energy is broken, as a result of the broken lattice translational symmetry. As shown in Fig. 2, the topological region corresponding to $W = +1$ drastically shrinks to a small region with the decrease of β, and eventually vanishes for $\beta \leqslant 1$. The topological region of the branch with $W = -1$ is converted into a topological phases with $W = -1/2$ after entering the long-range sector, which is similar to a long-range Kitaev chain. For a Kitaev chain with long-range pairing interactions, it is found in previous studies that an unconventional topolog-

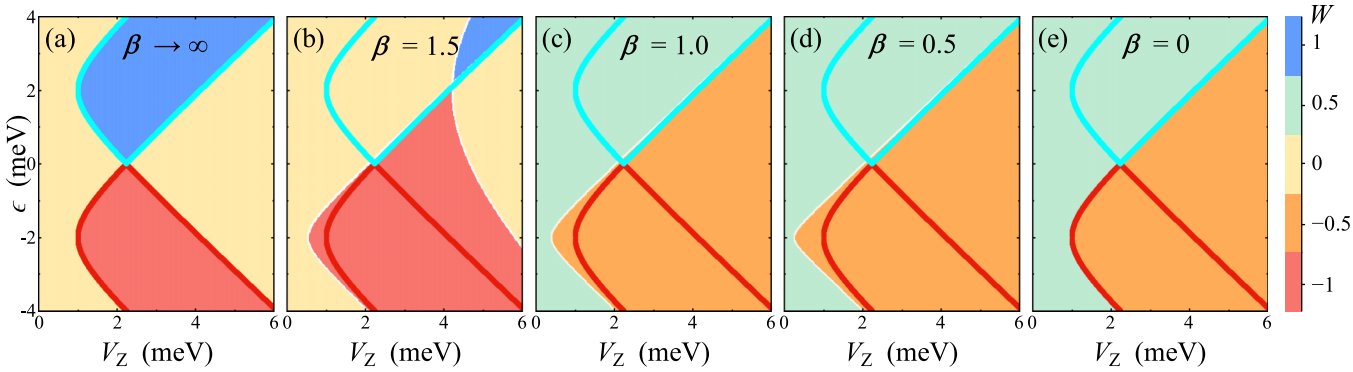

FIG. 2. Phase diagrams shown as a function of on-site energy ϵ and Zeeman splitting energy V_Z with power-law decaying long-range pairing interactions. (a)–(e) $\beta = \infty$, 1.5, 1.0, 0.5, and 0 correspond to the short-range limit, weak short-range regime, critical line, strong long-range regime, and the long-range limit, respectively. The yellow, blue, and red colored regions highlight the trivial and different topological phases indicated by the integer winding numbers $W = 0$, $W = +1$, and $W = -1$ in the short-range sector ($\beta > 1$). The topologically trivial and nontrivial phases in the long-range sector ($\beta \leqslant 1$) labeled by noninteger winding numbers are colored green and orange, respectively. The topological phases in the absence of any long-range pairing interactions are shown as regions bounded by the cyan solid line ($W = +1$) and red solid line ($W = -1$). Here, we take $t = t_{SO} = \Delta_0 = 1.0$ meV for a clear view.

ical phase with a half-integer winding number appears due to the energy spectrum divergence of the system Hamiltonian [7–13]. In this unconventional topological phase, the system hosts a topological massive Dirac fermion at the chain ends. For a nanowire with long-range rate $\beta \leqslant 1$, the long-range topological phase with a half-integer winding number $W = -1/2$ and a trivial phase with $W = 1/2$ are divided by a boundary where $(\mu - 4t)^2 = V_Z^2 - \tilde{\Delta}_a^2(\pi)$, as shown in Fig. 2. For $\beta > 1$, long-range interactions can significantly lower the threshold magnetic field for the emergence of MBSs [53]. In contrast, a long-range topological phase with $W = -1/2$ appearing at $\beta \leqslant 1$ indicates a nonmonotonic dependence as a function of decay rate β. The threshold Zeeman field supporting massive edge modes is significantly lowered with a decrease of β. With a further decrease of β, the threshold Zeeman field increases and approaches the value in the short-range pairing limit.

Figure 3 demonstrates the nonmonotonic dependence of the threshold Zeeman field on the decay rates of the long-range pairing more concisely. The enlargement of the topologically nontrivial region and the reduction of the threshold magnetic field induced by long-range interactions have been also demonstrated in several works [53–55]. Differently, it is shown in Fig. 3 that the threshold Zeeman field begins to increase as the decay rate β decreases for relatively small β. For $\beta = 0$ since the pairing strength between different sites is distance irrelevant, the threshold Zeeman field equals the value in the absence of a long-range pairing interaction. In this case, the lattice translational symmetry is restored again, leading to the symmetric phase diagram about the on-site energy $\epsilon = -2$ meV.

For comparison, the phase diagrams in the presence of an exponential decay of long-range pairing are illustrated in Fig. 4. The decay rate of the long-range pairing in this case is determined by the coherence length in the host superconductor. With the increase of the coherent length, the pairing strength between distant sites is considerably enhanced. It is shown in Fig. 4 that the effect of the exponential decay rate of long-range pairing on the phase diagram is qualitatively similar to the case of a power-law-type decay with $\beta > 1$. Long-range pairing with an exponential decay form can be derived from the weak coupling between the parent superconductor and the nanowire [53], which has the same long-range pairing form as that induced by magnetic impurities in helical Shiba chains. Different from the power-law decay pairing $\tilde{\Delta}_a(k)$ with $\beta \leqslant 1$, it can be deduced that the long-range pairing $\tilde{\Delta}_b(k)$ is always convergent. Therefore, there is no long-range topological phase in the presence of long-range pairing with an exponential decay rate. In this case, the threshold Zeeman field shows a monotonic dependence on

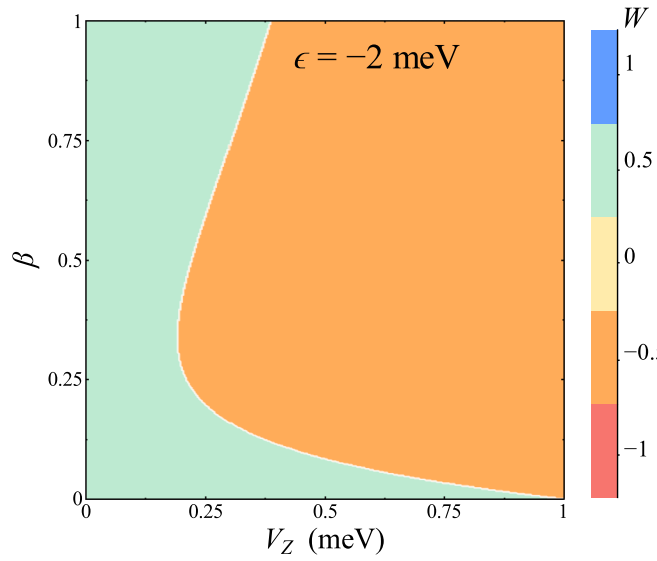

FIG. 3. Phase diagram as a function of the decay rate β and the Zeeman splitting energy V_Z at the low-field regime with on-site energy fixed at $\epsilon = -2$ meV. The critical line formed by the boundary between the unconventional topological phase (orange region) and the trivial phase (green region) indicates a nonmonotonic critical Zeeman splitting energy V_Z^C as β decreases from 1 towards 0. Other parameters are the same as in Fig. 2.

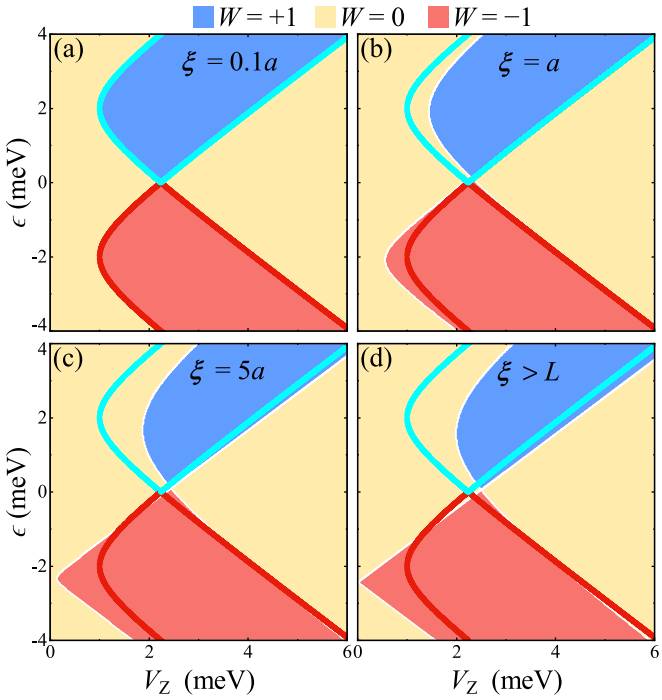

FIG. 4. Phase diagrams on the ϵ-V_Z plane of the nanowire with exponentially decaying long-range pairing interactions. (a)–(d) $\xi = 0.1a$, a, $5a$, and $\xi > L$ correspond to a short coherence length, a coherence length comparable with the lattice spacing, a coherence length larger than several lattice spacings, and the limit of long coherence length, respectively. Here, we set the Fermi momentum $k_F = \pi/2$ (half filling) and other parameters are the same as in Fig. 2.

the coherence length, different from the results of the power-law decay case.

We now turn to discuss the phase diagrams of the nanowire as functions of the chemical potential μ and the decay rate β of the long-range pairing. The results are shown in Fig. 5. For the long-range decay rate $\beta > 1$, two topological branches with opposite integer winding numbers $W = 1$ and $W = -1$

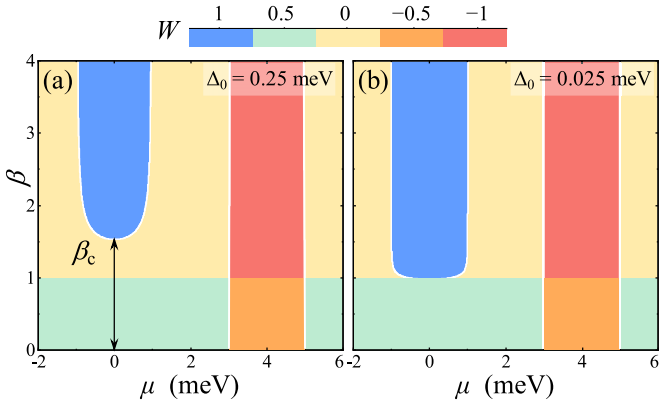

FIG. 5. Phase diagrams on the β-μ plane with power-law decaying long-range pairing exhibit a dependence on the on-site pairing potential. (a) $\Delta_0 = 0.25$ meV, (b) $\Delta_0 = 0.025$ meV. With chemical potential fixed at $\mu = 0$ ($\epsilon = 2t$), the topological phase transition occurs at $\beta = \beta_C$. The other parameters are $t = t_{SO} = V_Z = 1.0$ meV.

are asymmetrically distributed in the regimes of μ. The topological region with $W = 1$ vanishes for small decay rates. The critical decay rate approaches 1 for weak on-site pairing strength. The phase boundary with a winding number $W = 1$ depends on the value of on-site pairing Δ_0. Actually, it could be derived that $Z(\pi) > 0$ always holds for $|\mu| < 2t$. The expression for the winding number is thus simplified as

$$W = \tfrac{1}{2}\{1 - \mathrm{sgn}[\mu^2 + \widetilde{\Delta}_a^2(0) - V_Z^2]\}. \tag{29}$$

The condition for a nontrivial winding number is $V_Z > \sqrt{\mu^2 + \widetilde{\Delta}_a^2(0)}$. For $\mu = 0$, the condition is further simplified as

$$V_Z > \Delta_0 \left[1 + 2\sum_{r=1}^{L_c} (r+1)^{-\beta_C}\right], \tag{30}$$

where β_C represents the decay rate at the topological phase transition point. It is deduced that the critical decay rate β_C decreases with a decrease of Δ_0 for a fixed Zeeman field V_Z. Below the critical line $\beta = 1$ and in the thermodynamic limit ($L_c \to \infty$), the effective long-range pairing strength $\widetilde{\Delta}_a(0)$ becomes divergent and the system is driven into two new phases, corresponding to the half-integer winding numbers $W = \pm 1/2$. As illustrated in Fig. 5, the long-range topological phase with a half-integer winding number $W = -1/2$ appears in the region where $(\mu - 4t)^2 < V_Z^2 - \widetilde{\Delta}_a^2(\pi)$.

For a realistic nanowire, finite-size effects play an important role and a finite energy splitting could be generated by the hybridization between two well-localized edge states. Majorana energy splitting in a hybrid semiconductor-superconductor nanowire device has been demonstrated in several experiments [40]. In the Kitaev chain, a pair of massive edge modes could be induced for small decay rates of long-range pairing [7–11]. In the following, we resort to the exact diagonalization method for a lattice model and provide further insights into the effect of the long-range pairing interaction.

The full energy spectrum can be obtained by exactly diagonalizing the tight-binding Hamiltonian in Eq. (5). The energy spectra for a finite nanowire with long-range pairing terms are depicted in Fig. 6 as a function of the chemical potential μ. For $\beta > \beta_C$, it is demonstrated that MBSs appear in the region $\mu^2 < V_Z^2 - \widetilde{\Delta}_a^2(0)$ and $(\mu - 4t)^2 < V_Z^2 - \widetilde{\Delta}_a^2(\pi)$, corresponding to topological phases with integer winding numbers $W = \pm 1$, respectively. With a decrease of β, MBSs appear only in the region of $(\mu - 4t)^2 < V_Z^2 - \widetilde{\Delta}_a^2(\pi)$ for $1 < \beta < \beta_C$, while for another original topological region with $W = 1$, a finite energy gap is induced by the long-range pairing in the spectrum and the system is driven into a topological trivial phase. In this region, the energy gap becomes larger with the decreasing of β. In the long-range case $\beta \leqslant 1$, there is no essential difference in the energy spectra compared to the case of $\beta > 1$. However, in the region $(\mu - 4t)^2 < V_Z^2 - \widetilde{\Delta}_a^2(\pi)$, the near-zero-energy modes are the massive edge modes in the long-range topological phase, while not the MBSs. With a further decrease of β, it is noted that the energy gap in the spectrum is considerably suppressed within the nontopological region $\mu^2 < V_Z^2 - \Delta_0^2$. As illustrated in Fig. 6(f), the near-zero-energy ABSs in the topologically trivial phase are generated for sufficiently small decay rates. In particular, the

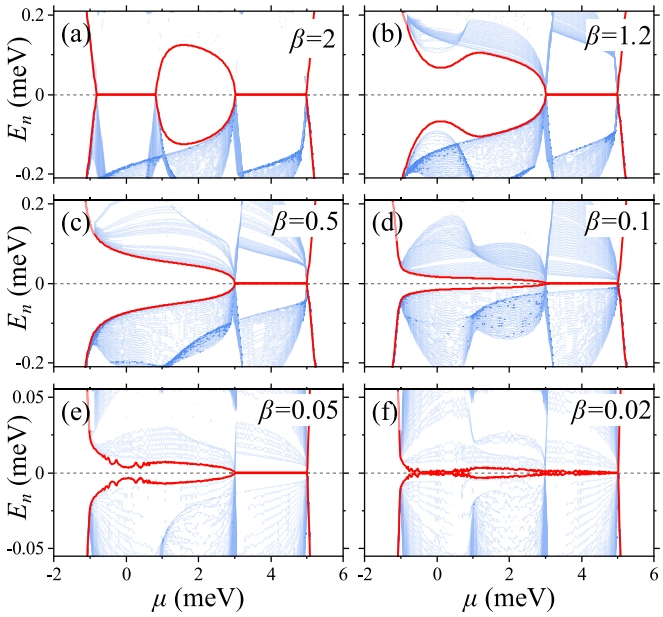

FIG. 6. The energy spectra for a finite Majorana nanowire with power-law decaying long-range pairing terms as a function of the chemical potential μ at various decay rates (a)–(f) $\beta = 2$, 1.2, 0.5, 0.1, 0.05, and 0.02. The energies for the lowest-lying states are colored red. We choose $L = 10$ μm and other parameters are the same as in Fig. 5(a).

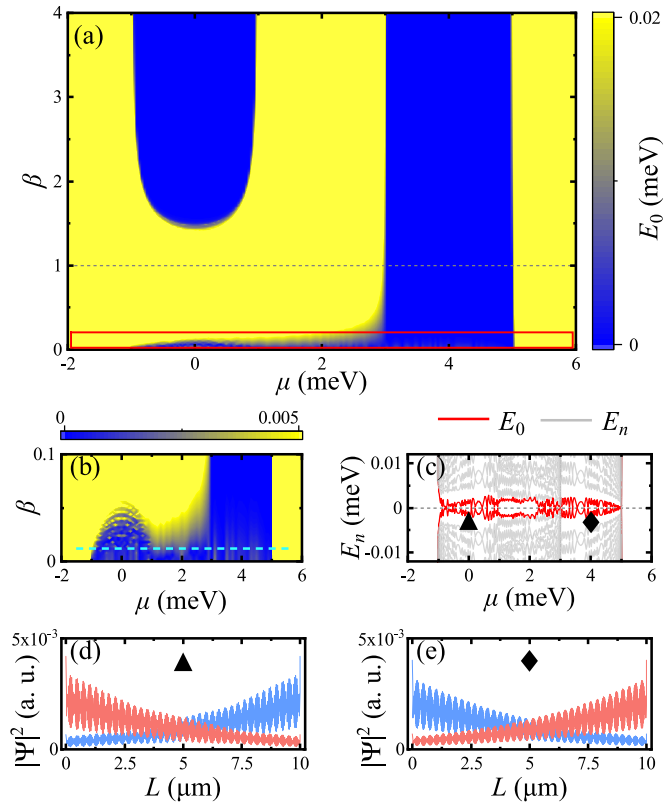

FIG. 7. The lowest-energy spectrum on a β-μ plane with power-law decaying long-range pairing. (a) Zeeman field fixed at $V_Z = 1.0$ meV and wire length $L = 4$ μm. (b) Details of the region bounded by the red box in (a) with a longer wire $L = 10$ μm. The cyan dashed line indicates where the cut in (c) is taken. (c) The energy of the lowest-lying state E_0 (red solid line) and the first few excited states E_n (gray solid line) vs the chemical potential μ at $\beta = 0.01$. (d), (e) The spatial profiles of the lowest-energy states marked by the triangle and diamond symbols in (c). Other parameters are the same as in Fig. 5.

massive edge modes in the topological phase with $W = -1/2$ and the ABSs in the trivial phase with $W = 1/2$ exhibit similar oscillatory energy-splitting behaviors, as a result of the finite-size effect.

Figure 7 illustrates the dependence of the lowest positive energy on the chemical potential and the decay rate of the long-range pairing interaction. To suppress the finite-size effect, a relatively long nanowire is chosen to weaken the energy splitting induced by the hybridization of two edge states at the wire ends. It is shown in Fig. 7 that in most regions, the distribution of the lowest positive energy is consistent with the phase diagram presented in Fig. 5(a). For instance, the near-zero-energy bound states always appear in the topological regions with $W = \pm 1$ and $W = -1/2$. The lowest-energy distribution contains more abundant information than the phase diagram. An important difference between them is that when the decay rate of the long-range pairing interaction is weak enough, the near-zero-energy ABSs emerge in the topologically trivial regime with $W = 1/2$. As shown in Fig. 7(b), these trivial bound states exist only in a very narrow region, where the strength of long-range pairing almost does not decay along the nanowire.

The energy of these trivial bound states does not strictly equal zero, and it fluctuates around the zero energy as a function of the chemical potential. Figure 7(c) illustrates that the topological massive edge modes in the $W = -1/2$ phase also exhibit similar oscillatory behavior. Figures 7(d) and 7(e) further demonstrate the similarity of the wave function for these two types of bound states. Different from the MBSs in the short-range regime $\beta > 1$, the wave functions of these near-zero-energy bound states are not well localized at the wire ends. For MBSs, the spatial distribution of the wave function is exponentially suppressed along the nanowire. On the contrary, the wave functions of these near-zero-energy bound states appearing in the long-range regime decay rather slowly, leading to a finite energy splitting even for a relatively long nanowire.

IV. TRANSPORT PROPERTIES

For the Kitaev chain, the long-range pairing interaction could induce a topological phase with a half-integer winding number, manifesting itself as a pair of massive edge modes whose finite overlapping survives even in the thermodynamic limit [7–13]. It is an important issue to distinguish Majorana zero modes from the massive edge modes. It is a natural choice to detect the inner physics through the transport measurement in a junction consisting of a long-range Kitaev chain contacting two normal metal leads. It was suggested by Giuliano *et al.* that the Fano factor of the shot noise could serve as a probe to discriminate these two bound states [25]. When the leads are biased at a voltage with respect to the superconducting chain, a nonzero noise Fano factor is induced by the mas-

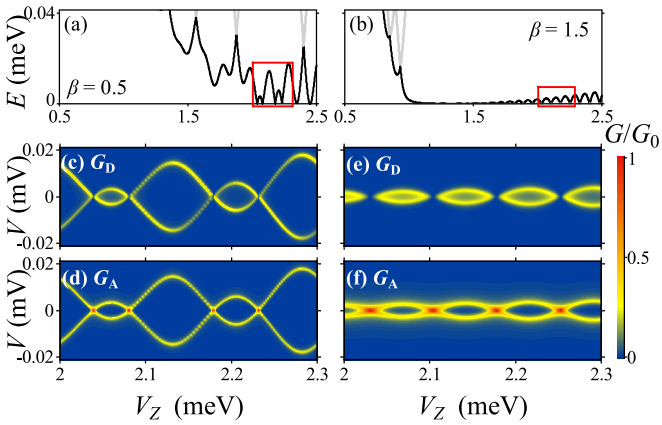

FIG. 8. Differential conductance as a function of the bias voltage V and Zeeman splitting energy V_Z for a Majorana nanowire with power-law decaying long-range pairing at (a) $\beta = 0.5$ and (b) $\beta = 1.5$. (c), (d) G_D and G_A are the conductances associated with the direct tunneling process and the local Andreev reflection, respectively. The extent of V_Z is indicated by the red box in (a). (e), (f) The same quantities plotted within the range of V_Z specified by the red box of (b). $G_0 = 2e^2/h$ is the quantized conductance. The system parameters are taken as $L = 2\ \mu$m, $t = 3$ meV, $\Delta_0 = 0.25$ meV, $\alpha = 0.1$ eV Å, $\mu = 0$, and $\Gamma_L = \Gamma_R = 0.05$ meV.

sive edge modes in the long-range topological phase, while for a Majorana zero mode, the Fano factor approaches zero.

It is shown in Fig. 7 that the ABSs and the massive edge modes with rather small energy splitting could be induced by the long-range pairing interaction in the trivial regime and the long-range topological phase, corresponding to the half-integer winding numbers $W = 1/2$ and $W = -1/2$, respectively. Different from an ideal long-range Kitaev chain that supports exact Majorana zero modes, there exists a finite energy splitting for both the MBSs and ABSs due to the finite-size effect in a realistic nanowire. It is questionable whether the transport measurement in a realistic nanowire device can provide useful information to distinguish the MBSs and ABSs. We consider a transport setup where a nanowire with a long-range pairing interaction is weakly coupled to two normal metal leads. The device parameters are chosen as $t = 3$ meV, $\Delta_0 = 0.25$ meV, $\alpha = 0.1$ eV Å, $\mu = 0$, and $\Gamma_L = \Gamma_R = 0.05$ meV, which are based on the typical values reported by relevant experiments [34,40,41,69,70]. It is noted that for a realistic nanowire, $t \gg \Delta_0$, and the long-range topological phase is difficult to realize for $\beta \leqslant 1$ in real nanowire devices.

First, we investigate the influence of long-range pairings on the differential conductance in both the topological and trivial cases. For comparison, we separately consider the contribution of different tunneling processes. Because the symmetric bias voltage $V_L = -V_R = V/2$ is applied, the current component I_{CA} contributed by the crossed Andreev reflection vanishes in this case, which can be deduced from Eq. (27). Figures 8(a) and 8(b) show the oscillatory energy splitting for the trivial ABS in the long-range regime ($\beta = 0.5$) and the MBSs in the short-range regime ($\beta = 1.5$), respectively. The corresponding conductance components G_D and G_A are illustrated in Figs. 8(c)–8(f), which are contributed by the direct tunneling and local Andreev reflection processes, respectively. It is demonstrated in Fig. 8 that the conductance components G_D and G_A are irrelevant to the types of bound states, but are sensitive to the energy splitting. The conductance peaks appear when the bias voltage equals the energy splitting, and indicate a similar oscillation as the energy splitting. When the energy splitting approaches zero, it is demonstrated in Fig. 8 that the conductance peak of G_D is considerably suppressed, while the peak of G_A is enhanced. In this case, the direct transport of electrons via the ABSs or MBSs is suppressed and the local Andreev reflection dominates the tunneling process.

The relationship between the lowest positive energy levels and the noise Fano factor of the system is demonstrated in Fig. 9 as a function of the Zeeman field. Both the MBSs and ABSs appearing in the topological nontrivial and trivial regimes are considered, respectively. Figure 9(a) indicates the dependence of the phase diagram on the Zeeman field and the decay rates of the long-range pairing. It is shown that the topological phase hosting MBSs is absent for weak decay rates $\beta < 1$ of the long-range pairing. To investigate the shot noise signature in different regimes, we separately consider three long-range decay rates of $\beta = 1.5$, 1.0, and 0.5. For the relatively strong decay rate $\beta = 1.5$, the topological property of the system is similar to an ordinary nanowire without a long-range pairing interaction. In this short-range case, the nanowire experiences a topological phase transition for a critical Zeeman field, and a pair of MBSs appear in two wire ends for $V_Z > V_Z^C$. In the opposite case where $\beta = 0.5$, the topological phase is considerably suppressed by the strong long-range effect and is absent in a wide range of the Zeeman field. There are no topological bound states existing in this case.

Because the near-zero-energy bound states appearing in the topological trivial phase are not reflected in the phase diagram, the energy spectra are plotted as a function of the Zeeman field for different long-range pairing regimes. It is illustrated in Fig. 9 that the oscillation of the low-energy bound states could be induced both in the topological nontrivial and trivial phases. It is deduced from the phase diagram that only the low-energy spectrum shown in Fig. 9 is MBSs, while the near-zero-energy states appearing for $\beta = 1.0$ and 0.5 are trivial ABSs. Compared with trivial ABSs shown in Fig. 9, the MBSs indicate more stable periodicity and increase gradually as a function of the Zeeman field.

The noise Fano factor as a function of the Zeeman field are presented in Figs. 9(e)–9(g), corresponding to the decay exponents at $\beta = 1.5$, 1, and 0.5, respectively. It is clearly shown that the behavior of the Fano factor is closely related to the energy spectrum of the bound states. When the Zeeman field varies, the noise Fano factor indicates a similar oscillation as the energy spectrum. As the bound state energy approaches zero, the Fano factor at the same V_Z drops to zero value. The Fano factor indicates a synchronic dependence on the bound state energy. As illustrated in Fig. 9, there is no difference in the Fano factor behavior between the transport properties of the topological MBSs and the trivial ABSs. It is difficult to distinguish MBSs and ABSs in a realistic nanowire by measuring the shot noise properties.

The irrelevance between the shot noise and the topological property of the system does not contradict the previous results

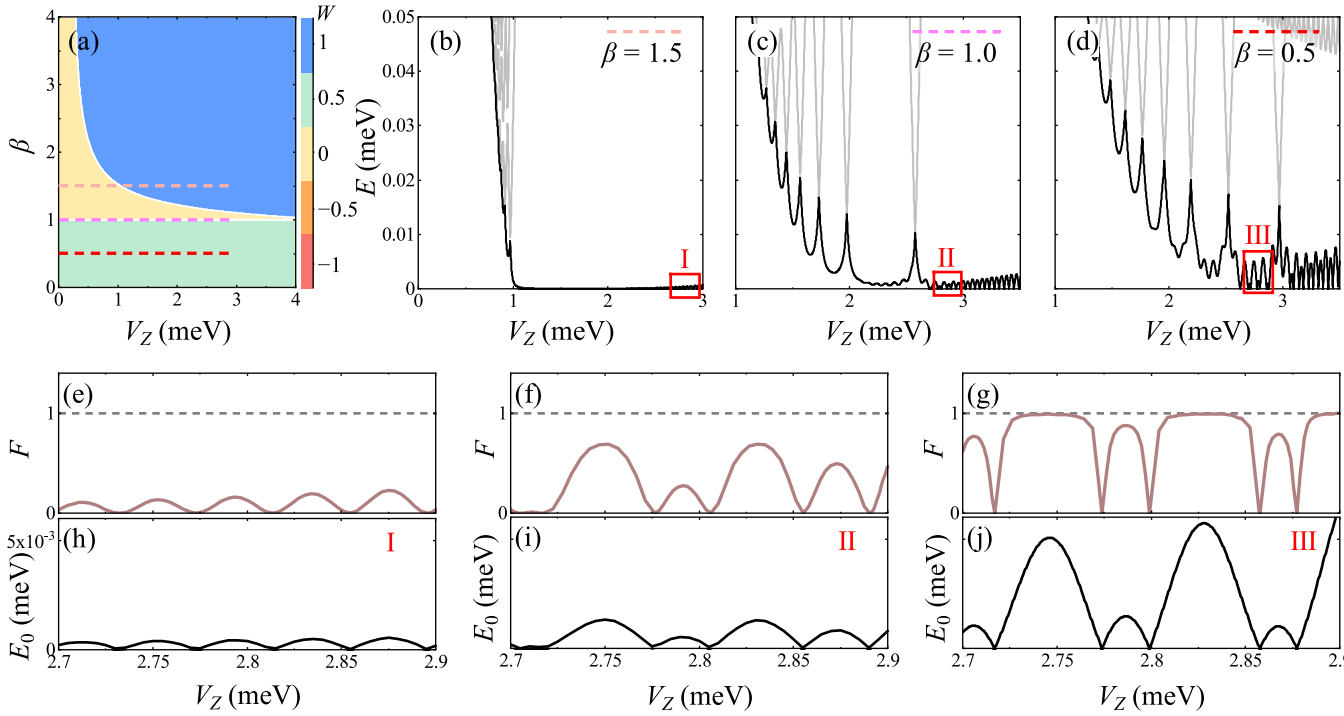

FIG. 9. Dependence of the shot noise Fano factors and low-energy spectrum on the Zeeman field in the presence of power-law decaying long-range pairing. (a) The phase diagram on the β-V_Z plane. The colored dashed lines correspond to the cuts where (b)–(d) are taken. (b)–(d) The low-energy spectrum as a function of Zeeman splitting energy V_Z for $\beta = 1.5$, $\beta = 1.0$, and $\beta = 0.5$, respectively. (e)–(g) The noise Fano factor as a function of V_Z and (h)–(j) the lowest energy vs V_Z in the ranges denoted by I, II, and III in the upper panels (bounded in red boxes). The system parameters are taken as those in Fig. 8 and the wire length is taken as $L = 4$ μm.

in a long-range Kitaev chain. In previous studies, an extended Kitaev chain with a long enough length was considered [25]. In this case, the hybridization of the MBSs localized in two wire ends is ignorable and the energy splitting approaches zero, resulting in a zero Fano factor. For the phase with a one-half winding number, there always exists a finite energy for the massive edge states, which corresponds to a nonzero Fano factor. The values of the noise Fano factor and the bound state energy are mainly determined by the hybridization of the edge states. Regardless of MBSs or trivial ABSs, the exact zero-energy modes facilitate the local Andreev reflection in the transport. Due to the absence of hybridization between two edge states, an injecting electron from one lead transfers $2e$ into the scattering region and a reflecting hole in the same lead. The exact zero-energy mode leads to the full suppression of the shot noise. However, the partial overlap between the edge modes allows a crossed Andreev reflection, in which the incoming electron from one lead turns into an outgoing hole in the other lead. Therefore, a finite energy splitting corresponds to a nonzero noise Fano factor, and the shot noise is not related to the topological property of the system.

Finally, we discuss the effect of the long-range pairing with an exponential decay form on the Fano factor of the shot noise. In Fig. 10 we present the energy spectrum and the noise Fano factor as a function of the Zeeman field in the presence of an exponentially decayed long-range pairing term. The results in the topological nontrivial phase and trivial phase are illustrated in Figs. 10(a) and 10(b) and Figs. 10(c) and 10(d), respectively. As shown in Fig. 10, the noise Fano factor behaves similarly to that in the case of a power-law decay. The negligible hybridizations between two edge modes result in zero Fano factors, while a finite energy splitting by the hybridization always leads to a nonzero Fano factor. The noise Fano factor and the lowest positive energy splitting directly manifest the hybridization strength. In the topological trivial regime, no near-zero-energy ABSs are induced in this case and the Fano factor F approaches 2, reflecting the transmission of Cooper pairs through the device [68]. The results shown in Fig. 10 are qualitatively consistent with those of a power-law-type decay. Although the noise Fano factor is irrelevant to the topological property of the system, it could serve as a good probe to detect the energy splitting of the low-energy bound states in the superconducting gap.

V. CONCLUSIONS

In conclusion, we investigate the phase diagram and the quantum transport properties in a semiconductor-superconductor hybrid nanowire by taking into account the long-range pairing interactions. We separately consider two cases where the long-range pairing is the power law and exponentially decayed with the distance. Although long-range pairing with an exponential decay rate could be derived in a realistic device, the power-law decayed form is widely adopted and investigated in the extended Kitaev chain models. The general expressions for the winding number and the transport quantities including the current and shot noise are derived. For a long-range pairing with a power-law decay rate, it is found that the threshold magnetic field for the emergence of MBSs indicates a nonmonotonic dependence on the decay

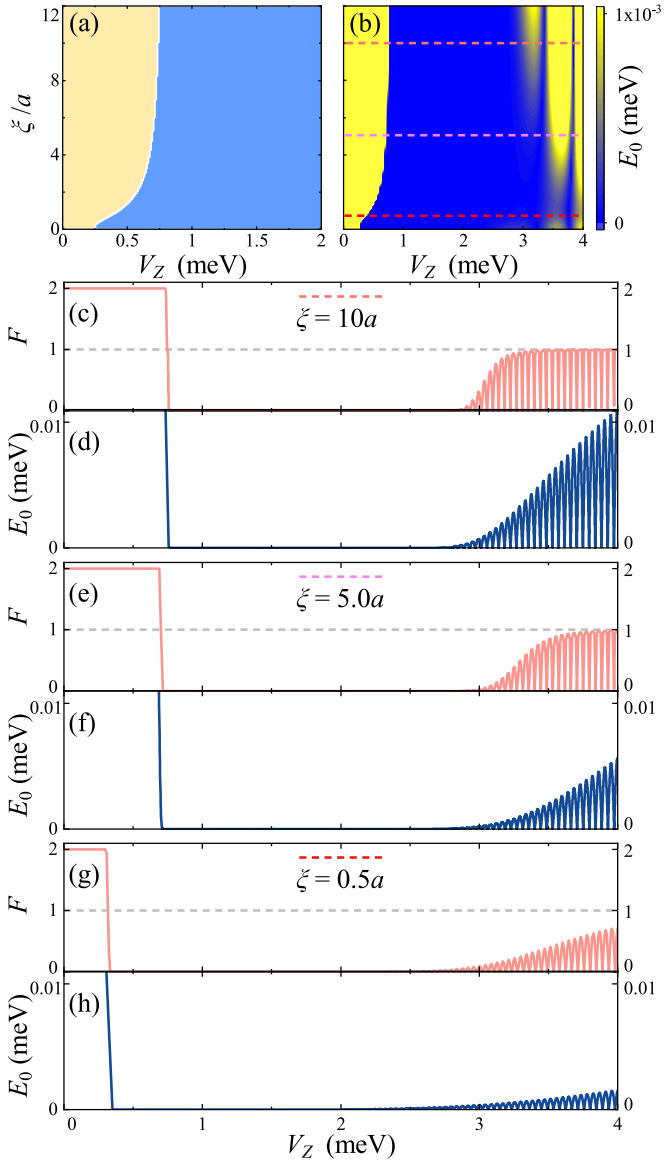

FIG. 10. The phase diagram, the lowest energy, and shot noise Fano factor as a function of Zeeman splitting energy V_Z and coherence length ξ in the presence of exponentially decaying long-range pairing interactions. (a), (b) The phase diagram and the lowest-energy spectrum on the ξ-V_Z plane. The dashed lines indicate where the cuts in the lower panels are taken. (c) and (d) illustrate the orange line cut of (b) and the corresponding shot noise Fano factor against V_Z at $\xi = 10a$. Similarly, (e), (f) and (g), (h) plot the pink and red line cuts and the corresponding Fano factors as functions of V_Z for $\xi = 5a$ and $\xi = 0.5a$, respectively. Other parameters are the same as in Fig. 9.

rates. The threshold Zeeman field is significantly lowered for a moderate decay rate. As the exponent of the power-law decay in the long-range pairing is less than one, a long-range topological phase hosting massive edge modes is induced. For a weak enough decay rate, the threshold Zeeman field increases and is restored to the value in the short-range pairing limit. Differently, for the exponential decay form, the threshold magnetic field becomes weaker when long-range pairing decays more slowly. Because the low-energy bound states cannot be captured in the phase diagram, we also perform the exact diagonalization calculations for the tight-binding Hamiltonian to obtain the energy spectrum of the system. It is found that near-zero-energy ABSs could be induced in a topologically trivial phase for slowly decayed long-range pairing interactions.

For a one-dimensional Kitaev chain with long-range pairing, the Fano factor of the shot noise is suggested to serve as a probe to discriminate the topological property of the system. Our numerical results indicate that regardless of the MBSs and the trivial ABSs, the noise Fano factor is generally consistent with the variation of the bound state energy. However, the noise Fano factor is irrelevant to the topological property of the system and fails to distinguish these two bound states. It is noted that this irrelevance does not contradict the previous studies, in which a Kitaev chain with a long enough length is considered. In this case, the Majorana energy splitting approaches zero and crossed Andreev reflection is fully suppressed, corresponding to a zero Fano factor. For the massive edge states appearing in the phase with one-half winding number, there always exists a finite energy splitting, leading to a nonzero Fano factor. The values of the noise Fano factor and the bound state energy are mainly determined by the hybridization of the edge states. Therefore, although the noise Fano factor cannot be used to distinguish the MBSs and ABSs, it is a sensitive probe to detect the energy splitting of these bound states.

ACKNOWLEDGMENTS

This work was supported by the Natural Science Foundation of China under Grants No. 12074209 and No. 61474018, the Fundamental Research Funds for the Central Universities (No. ZYGX2019J100), and the Open Project of State Key Laboratory of Low-Dimensional Quantum Physics (Grant No. KF202008).

APPENDIX: DERIVATION OF THE TUNNELING CURRENT

In this Appendix, we start by first considering the tunneling current of a spinless model without any superconducting pairings and then deduce the current formula for the Majorana nanowire case. The average current I_γ flowing from the $\gamma = L, R$ lead into the wire is defined as

$$I_\gamma(t) = \langle -e\dot{N}_\gamma \rangle = \frac{ie}{\hbar}\langle [N_\gamma, H] \rangle, \tag{A1}$$

where $N_\gamma = \sum_k d^\dagger_{k\gamma} d_{k\gamma}$ is the number operator for the γ lead and $d_{k\gamma}$ ($d^\dagger_{k\gamma}$) annihilates (creates) an electron of state k in the normal lead. The total Hamiltonian of the system can be decomposed into three components,

$$H_L = \sum_{k\gamma} \epsilon_{k\gamma} d^\dagger_{k\gamma} d_{k\gamma}, \tag{A2}$$

$$H_T = \sum_{k\gamma,n} t_{k\gamma,n} d^\dagger_{k\gamma} c_n + \text{H.c.}, \tag{A3}$$

$$H_C = \sum_{ij} h_{ij} c^\dagger_i c_j + \text{H.c.} \tag{A4}$$

Here, H_L, H_T, and H_C describe the leads, the lead-wire couplings, and the central region, respectively. c_i is the annihilation operator on site i of the nanowire wire. c_n annihilates electrons at the two ends of wire, i.e., $n = 1, N$ for $\gamma = L, R$ and N is the site numbers. The lead-wire coupling between the γ lead and the site n is denoted by $t_{k\gamma,n}$. h_{ij} captures the generic hopping terms between site i and j in the wire. Since N_γ commutes with H_L and H_C, combining with $[d_k^\dagger d_k, d_{k'}^\dagger c_i] = d_k^\dagger c_i \delta_{kk'}$ and $[d_k^\dagger d_k, c_i^\dagger d_k'] = -c_i^\dagger d_k \delta_{kk'}$, Eq. (A1) can be further expressed as

$$\begin{aligned} I_\gamma(t) =& \frac{ie}{\hbar}\langle [N_\gamma, H_T]\rangle \\ =& \frac{ie}{\hbar}\sum_{k;k'\gamma'} t_{k'\gamma',n}\langle [d_{k\gamma}^\dagger d_{k\gamma}, d_{k'\gamma'}^\dagger c_n]\rangle \\ &+ t_{k'\gamma',n}^*\langle [d_{k\gamma}^\dagger d_{k\gamma}, c_n^\dagger d_{k'\gamma'}]\rangle \\ =& \frac{ie}{\hbar}\sum_k t_{k\gamma,n}\langle d_{k\gamma}^\dagger c_n\rangle - t_{k\gamma,n}^*\langle c_n^\dagger d_{k\gamma}\rangle. \end{aligned} \tag{A5}$$

Note that in the Keldysh formalism, the lesser Green's function is defined as the following correlation functions,

$$G_{n,k\gamma}^<(t,t') \equiv i\langle d_{k\gamma}^\dagger(t') c_n(t)\rangle, \tag{A6}$$

$$G_{k\gamma,n}^<(t,t') \equiv i\langle c_n^\dagger(t') d_{k\gamma}(t)\rangle. \tag{A7}$$

Insert back into Eq. (A5) and use the relation $G_{n,k\gamma}^<(t,t') = -G_{k\gamma,n}^<(t,t')^\star$, we have

$$\begin{aligned} I_\gamma(t) =& \frac{e}{\hbar}\sum_k t_{k\gamma,n} G_{n,k\gamma}^<(t,t') - t_{k\gamma,n}^* G_{k\gamma,n}^<(t,t') \\ =& \frac{2e}{\hbar}\mathrm{Re}\sum_k t_{k\gamma,n} G_{n,k\gamma}^<(t,t'). \end{aligned} \tag{A8}$$

To obtain the expression of $G_{k\gamma,\gamma}^<(t,t')$, we apply the Langreth analytic continuation rules on the Keldysh contour,

$$\begin{aligned} G_{n,k\gamma}^<(t,t') = \sum_m \int dt_1 t_{k\gamma,m}^\star \big[& G_{nm}^r(t,t_1) g_{k\gamma}^<(t_1,t') \\ &+ G_{nm}^<(t,t_1) g_{k\gamma}^a(t_1,t')\big], \end{aligned} \tag{A9}$$

where G_{nm}^r is the retarded Green's function for the wire and $g^{<(r,a)}$ are the Green's functions accounting for the leads:

$$g_{k\gamma}^<(t,t') \equiv i\langle d_{k\gamma}^\dagger(t') d_{k\gamma}(t)\rangle, \tag{A10}$$

$$g_{k\gamma}^{r,a}(t,t') \equiv \mp i\theta(\pm t \mp t')\langle\{d_{k\gamma}(t), d_{k\gamma}^\dagger(t')\}\rangle. \tag{A11}$$

Then we can Fourier transform Eq. (A9) into the energy domain as

$$G_{n,k\gamma}^<(\omega) = \textstyle\sum_m t_{k\gamma,m}^\star \big[G_{nm}^r(\omega) g_{k\gamma}^<(\omega) + G_{nm}^<(\omega) g_{k\gamma}^a(\omega)\big]. \tag{A12}$$

By substituting Eq. (A12) into Eq. (A8) we have

$$\begin{aligned} I_\gamma =& \frac{2e}{\hbar}\int \frac{d\omega}{2\pi}\mathrm{Re}\sum_{k,nm} t_{k\gamma,n} t_{k\gamma,m}^* \big[G_{nm}^r(\omega) g_{k\gamma}^<(\omega) + G_{nm}^<(\omega) g_{k\gamma}^a(\omega)\big] \\ =& \frac{2e}{\hbar}\int \frac{d\omega}{2\pi}\mathrm{Re}\sum_{nm} G_{nm}^r(\omega)\left[\sum_k t_{k\gamma,n} g_{k\gamma}^<(\omega) t_{k\gamma,m}^*\right] + G_{nm}^<(\omega)\left[\sum_k t_{k\gamma,n} g_{k\gamma}^a(\omega) t_{k\gamma,m}^*\right] \\ =& \frac{2e}{h}\int d\omega\,\mathrm{Re}\sum_{nm} G_{nm}^r(\omega)\Sigma_{\gamma,mn}^<(\omega) + G_{nm}^<(\omega)\Sigma_{\gamma,mn}^a(\omega), \end{aligned} \tag{A13}$$

where we use the definitions of self-energies for lead γ,

$$\Sigma_{\gamma,mn}^<(\omega) \equiv \sum_k t_{k\gamma,n} g_{k\gamma}^<(\omega) t_{k\gamma,m}^*, \tag{A14}$$

$$\Sigma_{\gamma,mn}^a(\omega) \equiv \sum_k t_{k\gamma,n} g_{k\gamma}^a(\omega) t_{k\gamma,m}^*. \tag{A15}$$

Note that the current density in Eq. (A13) can be expanded as

$$\begin{aligned} \mathcal{I}_\gamma(\omega) = \frac{e}{h}\sum_{nm}\big[& G_{nm}^r(\omega)\Sigma_{\gamma,mn}^<(\omega) - \Sigma_{\gamma,nm}^<(\omega) G_{mn}^a(\omega) \\ &+ G_{nm}^<(\omega)\Sigma_{\gamma,mn}^a(\omega) - \Sigma_{\gamma,nm}^r(\omega) G_{mn}^<(\omega)\big]. \end{aligned} \tag{A16}$$

This result can be further expressed in matrix form where we drop the subscripts to denote matrices,

$$\begin{aligned} \mathcal{I}_\gamma(\omega) =& \frac{e}{h}\mathrm{Tr}\big[G^r(\omega)\Sigma_\gamma^<(\omega) - \Sigma_\gamma^<(\omega) G^a(\omega) \\ &+ G^<(\omega)\Sigma_\gamma^a(\omega) - \Sigma_\gamma^r(\omega) G^<(\omega)\big] \\ =& \frac{e}{h}\mathrm{Tr}\big[-i\Sigma_\gamma^<(\omega) i[G^r(\omega) - G^a(\omega)] \\ &+ i\big[\Sigma_\gamma^a(\omega) - \Sigma_\gamma^r(\omega)\big][-iG^<(\omega)]\big] \\ =& \frac{e}{h}\mathrm{Tr}\big[\Sigma_\gamma^{in}(\omega) A(\omega) - \Gamma_\gamma(\omega) G^n(\omega)\big], \end{aligned} \tag{A17}$$

where the second equality holds since $\mathrm{Tr}[AB] = \mathrm{Tr}[BA]$. For a more compact expression we introduce the following notations,

$$G^n \equiv -iG^<, \tag{A18}$$

$$\Sigma_\gamma^{in} \equiv -i\Sigma_\gamma^<, \tag{A19}$$

$$A \equiv i[G^r - G^a], \tag{A20}$$

$$\Gamma_\gamma \equiv i\big[\Sigma_\gamma^a - \Sigma_\gamma^r\big]. \tag{A21}$$

By the Dyson equation and definitions of retarded and advanced Green's function of the central region,

$$G^r = [\epsilon - H_C - \Sigma^r]^{-1},$$
$$G^a = (G^r)^\dagger,$$

we have

$$(G^r)^{-1} - (G^a)^{-1} = \Sigma^r - \Sigma^a = i\Gamma, \quad A \equiv i[G^r - G^a]$$
$$= iG^r[(G^a)^{-1} - (G^r)^{-1}]G^a = G^r\Gamma G^a,$$

where $\Sigma^{r(a)} = \Sigma_L^{r(a)} + \Sigma_R^{r(a)}$, $\Gamma = \Gamma_L + \Gamma_R$. Combining with the relations

$$G^n = G^r\Sigma^{in}G^a,$$
$$\Sigma^{in}(\omega) = \sum_\gamma \Sigma_\gamma^{in}(\omega) = \sum_\gamma \Gamma_\gamma(\omega)f_\gamma(\omega),$$

where $f_\gamma(\omega)$ denotes the Fermi-Dirac distribution for lead γ. We can further express Eq. (A17) as

$$\begin{aligned}\mathcal{I}_\gamma(\omega) &= \frac{e}{h}\mathrm{Tr}\big[\Sigma_\gamma^{in}(\omega)A(\omega) - \Gamma_\gamma(\omega)G^n(\omega)\big] \\ &= \frac{e}{h}\mathrm{Tr}[\Gamma_\gamma(\omega)f_\gamma(\omega)G^r(\omega)[\Gamma_L(\omega) + \Gamma_R(\omega)]G^a(\omega) \\ &\quad - \Gamma_\gamma(\omega)G^r(\omega)[\Gamma_L(\omega)f_L(\omega) + \Gamma_R(\omega)f_R(\omega)]G^a(\omega)] \\ &= \frac{e}{h}\mathrm{Tr}[\Gamma_L(\omega)G^r(\omega)\Gamma_R(\omega)G^a(\omega)][f_L(\omega) - f_R(\omega)].\end{aligned} \tag{A22}$$

Now we calculate the tunneling current for the Majorana nanowire case. With the Nambu spinor $\psi_k^\dagger = [c_{k\uparrow}^\dagger, c_{k\downarrow}^\dagger, c_{-k\uparrow}, c_{-k\downarrow}]$, the number operator of lead γ now reads

$$\begin{aligned}N_\gamma &\equiv \sum_k d_{k\uparrow,\gamma}^\dagger d_{k\uparrow,\gamma} + d_{k\downarrow,\gamma}^\dagger d_{k\downarrow,\gamma} \\ &= \frac{1}{2}\sum_k [d_{k\uparrow,\gamma}^\dagger d_{k\uparrow,\gamma} + d_{k\downarrow,\gamma}^\dagger d_{k\downarrow,\gamma} \\ &\quad - d_{-k\uparrow,\gamma}d_{-k\uparrow,\gamma}^\dagger - d_{-k\downarrow,\gamma}d_{-k\downarrow,\gamma}^\dagger].\end{aligned} \tag{A23}$$

Following Eq. (A1), the total current from lead γ can then be calculated,

$$\begin{aligned}I_\gamma(t) &= \frac{ie}{h}\langle[N_\gamma, H]\rangle \\ &= \frac{ie}{2h}\big[\langle[d_{k\uparrow,\gamma}^\dagger d_{k\uparrow,\gamma}, H]\rangle + \langle[d_{k\downarrow,\gamma}^\dagger d_{k\downarrow,\gamma}, H]\rangle \\ &\quad - \langle[d_{-k\uparrow,\gamma}d_{-k\uparrow,\gamma}^\dagger, H]\rangle - \langle[d_{-k\downarrow,\gamma}d_{-k\downarrow,\gamma}^\dagger, H]\rangle\big] \\ &= \frac{1}{2}\big[I_\gamma^{e\uparrow} + I_\gamma^{e\downarrow} - I_\gamma^{h\uparrow} - I_\gamma^{h\downarrow}\big] \\ &= \frac{1}{2}\mathrm{Tr}[\widetilde{\tau}_z I_\gamma],\end{aligned} \tag{A24}$$

where the trace is taken over the Nambu space and $\widetilde{\tau}_z \equiv \mathbb{1}_{2N\times 2N} \otimes \tau_z$ accounts for the different charges carried by electrons and holes. The current operator in matrix form I_γ reads

$$I_\gamma = \frac{e}{h}\big[G^r\Sigma_\gamma^< - \Sigma_\gamma^< G^a + G^<\Sigma_\gamma^a - \Sigma_\gamma^r G^<\big]. \tag{A25}$$

Here, $G^{<(r/a)}$ and $\Sigma_\gamma^{<(r/a)}$ denote the matrix forms of the Green's functions and self-energies with the Nambu spinor chosen to be $\psi^\dagger = [c_{1\uparrow}^\dagger, \ldots, c_{N\downarrow}^\dagger, c_{1\uparrow}, \ldots, c_{N\downarrow}]$. They are given respectively as block matrices,

$$G^{<(r/a)} \equiv \begin{bmatrix} G_{ee}^{<(r/a)} & G_{eh}^{<(r/a)} \\ G_{he}^{<(r/a)} & G_{hh}^{<(r/a)} \end{bmatrix}, \tag{A26}$$

$$\Sigma_\gamma^{<(r/a)} \equiv \begin{bmatrix} \Sigma_{\gamma,ee}^{<(r/a)} & \Sigma_{\gamma,eh}^{<(r/a)} \\ \Sigma_{\gamma,he}^{<(r/a)} & \Sigma_{\gamma,hh}^{<(r/a)} \end{bmatrix}. \tag{A27}$$

Note that for a normal metallic lead, we have diagonal self-energies, namely, $\Sigma_{\gamma,he}^{<(r/a)} = \Sigma_{\gamma,eh}^{<(r/a)} = 0$ holds. This observation further simplifies the matrix product terms in Eq. (A25) to

$$\begin{aligned}G\Sigma &= \begin{bmatrix} G_{ee}\Sigma_{ee} + G_{eh}\Sigma_{he} & G_{ee}\Sigma_{eh} + G_{eh}\Sigma_{hh} \\ G_{he}\Sigma_{ee} + G_{hh}\Sigma_{he} & G_{he}\Sigma_{eh} + G_{hh}\Sigma_{hh} \end{bmatrix} \\ &= \begin{bmatrix} G_{ee}\Sigma_{ee} & G_{eh}\Sigma_{hh} \\ G_{he}\Sigma_{ee} & G_{hh}\Sigma_{hh} \end{bmatrix},\end{aligned} \tag{A28}$$

where we leave out other indices for brevity. Substituting this result into Eq. (A24), the total current from γ lead can be formulated as

$$\begin{aligned}I_\gamma &= \frac{e}{2h}\mathrm{Tr}\big[\big(G^r\Sigma_\gamma^< - \Sigma_\gamma^< G^a + G^<\Sigma_\gamma^a - \Sigma_\gamma^r G^<\big)_{ee} \\ &\quad - \big(G^r\Sigma_\gamma^< - \Sigma_\gamma^< G^a + G^<\Sigma_\gamma^a - \Sigma_\gamma^r G^<\big)_{hh}\big] \\ &\equiv \frac{e}{2h}\mathrm{Tr}\big[I_\gamma^{ee} - I_\gamma^{hh}\big],\end{aligned} \tag{A29}$$

where we use the notation $(AB)_{ee(hh)} \equiv A_{ee(hh)}B_{ee(hh)}$. Following a similar derivation developed in Eq. (A17), we can rewrite the total current for the Majorana nanowire in terms of notations given in Eq. (A18). In the Nambu space we have

$$\Gamma_{\gamma,ee(hh)} \equiv \Gamma_\gamma^{e(h)}, \tag{A30}$$

$$\Sigma_{\gamma,ee(hh)}^{in} \equiv \Gamma_\gamma^{e(h)} f_\gamma^{e(h)}, \tag{A31}$$

where $f_\gamma^{e(h)}(\omega) = 1/(1 + e^{(\omega \mp \mu_L)/k_BT})$ are the Fermi distribution functions of an electron and hole in the γ lead, respectively. The terms I_γ^{ee} and I_γ^{hh} in Eq. (A29) take the forms

$$\begin{aligned}I_\gamma^{ee} &= \big(G^r\Sigma_\gamma^< - \Sigma_\gamma^< G^a + G^<\Sigma_\gamma^a - \Sigma_\gamma^r G^<\big)_{ee} \\ &= \big[-i\Sigma_\gamma^< i(G^r - G^a) + i\big(\Sigma_\gamma^a - \Sigma_\gamma^r\big)(-iG^<)\big]_{ee} \\ &= \Gamma_\gamma^e f_\gamma^e\big[G^r\big(\Gamma_L^e + \Gamma_L^h + \Gamma_R^e + \Gamma_R^h\big)G^a\big]_{ee} - \Gamma_\gamma^e\big[G^r\big(\Gamma_L^e f_L^e + \Gamma_L^h f_L^h + \Gamma_R^e f_R^e + \Gamma_R^h f_R^h\big)G^a\big]_{ee} \\ &= \Gamma_\gamma^e\big(G^r\Gamma_{\bar{\gamma}}^e G^a\big)_{ee}\big(f_\gamma^e - f_{\bar{\gamma}}^e\big) + \Gamma_\gamma^e\big(G^r\Gamma_\gamma^h G^a\big)_{ee}\big(f_\gamma^e - f_\gamma^h\big) + \Gamma_\gamma^e\big(G^r\Gamma_{\bar{\gamma}}^h G^a\big)_{ee}\big(f_\gamma^e - f_{\bar{\gamma}}^h\big),\end{aligned} \tag{A32}$$

$$
\begin{aligned}
I_\gamma^{hh} &= \left(G^r\Sigma_\gamma^< - \Sigma_\gamma^< G^a + G^<\Sigma_\gamma^a - \Sigma_\gamma^r G^<\right)_{hh} \\
&= \Gamma_\gamma^h f_\gamma^h\left[G^r\left(\Gamma_L^e + \Gamma_L^h + \Gamma_R^e + \Gamma_R^h\right)G^a\right]_{hh} - \Gamma_\gamma^h\left[G^r\left(\Gamma_L^e f_L^e + \Gamma_L^h f_L^h + \Gamma_R^e f_R^e + \Gamma_R^h f_R^h\right)G^a\right]_{hh} \\
&= \Gamma_\gamma^h\left(G^r\Gamma_{\bar\gamma}^h G^a\right)_{hh}\left(f_\gamma^h - f_{\bar\gamma}^h\right) + \Gamma_\gamma^h\left(G^r\Gamma_\gamma^e G^a\right)_{hh}\left(f_\gamma^h - f_\gamma^e\right) + \Gamma_\gamma^h\left(G^r\Gamma_{\bar\gamma}^e G^a\right)_{hh}\left(f_\gamma^h - f_{\bar\gamma}^e\right),
\end{aligned}
\tag{A33}
$$

where $\gamma = L, R$ and $\bar\gamma = R, L$. Inserting Eqs. (A32) and (A33) back into Eq. (A29), we obtain the expression of current I_γ in the Nambu-spinor space as

$$
\begin{aligned}
I_\gamma = &\frac{e}{h}\int d\omega\left[T_D\left(f_\gamma^e - f_{\bar\gamma}^e\right) + T_A\left(f_\gamma^e - f_\gamma^h\right)\right. \\
&\left. + T_{CA}\left(f_\gamma^e - f_{\bar\gamma}^h\right)\right],
\end{aligned}
\tag{A34}
$$

where the transmission functions contributed by the direct tunneling process, the local Andreev reflection, and crossed Andreev reflection are given, respectively,

$$
\begin{aligned}
T_D &\equiv \mathrm{Tr}\left[\Gamma_\gamma^e G^r \Gamma_{\bar\gamma}^e G^a\right], \\
T_A &\equiv \mathrm{Tr}\left[\Gamma_\gamma^e G^r \Gamma_\gamma^h G^a\right], \\
T_{CA} &\equiv \mathrm{Tr}\left[\Gamma_\gamma^e G^r \Gamma_{\bar\gamma}^h G^a\right].
\end{aligned}
\tag{A35}
$$

This result is equivalent to Eq. (27) in Sec. II.

[1] D. A. Ivanov, Non-Abelian Statistics of Half-Quantum Vortices in p-Wave Superconductors, Phys. Rev. Lett. **86**, 268 (2001).

[2] A. Yu. Kitaev, Fault-tolerant quantum computation by anyons, Ann. Phys. **303**, 2 (2003).

[3] C. Nayak, S. H. Simon, A. Stern, M. Freedman, and S. Das Sarma, Non-Abelian anyons and topological quantum computation, Rev. Mod. Phys. **80**, 1083 (2008).

[4] S. D. Sarma, M. Freedman, and C. Nayak, Majorana zero modes and topological quantum computation, npj Quantum Inf. **1**, 15001 (2015).

[5] D. Aasen, M. Hell, R. V. Mishmash, A. Higginbotham, J. Danon, M. Leijnse, T. S. Jespersen, J. A. Folk, C. M. Marcus, K. Flensberg, and J. Alicea, Milestones Toward Majorana-Based Quantum Computing, Phys. Rev. X **6**, 031016 (2016).

[6] A. Y. Kitaev, Unpaired Majorana fermions in quantum wires, Phys. Usp. **44**, 131 (2001).

[7] D. Vodola, L. Lepori, E. Ercolessi, A. V. Gorshkov, and G. Pupillo, Kitaev Chains with Long-Range Pairing, Phys. Rev. Lett. **113**, 156402 (2014).

[8] D. Vodola, L. Lepori, E. Ercolessi, and G. Pupillo, Long-range Ising and Kitaev models: Phases, correlations and edge modes, New J. Phys. **18**, 015001 (2015).

[9] Z.-X. Gong, M. F. Maghrebi, A. Hu, M. L. Wall, M. Foss-Feig, and A. V. Gorshkov, Topological phases with long-range interactions, Phys. Rev. B **93**, 041102(R) (2016).

[10] O. Viyuela, D. Vodola, G. Pupillo, and M. A. Martin-Delgado, Topological massive Dirac edge modes and long-range superconducting Hamiltonians, Phys. Rev. B **94**, 125121 (2016).

[11] L. Lepori, D. Vodola, G. Pupillo, G. Gori, and A. Trombettoni, Effective theory and breakdown of conformal symmetry in a long-range quantum chain, Ann. Phys. **374**, 35 (2016).

[12] X. Cai, Disordered Kitaev chains with long-range pairing, J. Phys.: Condens. Matter **29**, 115401 (2017).

[13] A. Alecce and L. Dell'Anna, Extended Kitaev chain with longer-range hopping and pairing, Phys. Rev. B **95**, 195160 (2017).

[14] A. Dutta and A. Dutta, Probing the role of long-range interactions in the dynamics of a long-range Kitaev chain, Phys. Rev. B **96**, 125113 (2017).

[15] C. Li, X. Z. Zhang, G. Zhang, and Z. Song, Topological phases in a Kitaev chain with imbalanced pairing, Phys. Rev. B **97**, 115436 (2018).

[16] I. Mahyaeh and E. Ardonne, Zero modes of the Kitaev chain with phase-gradients and longer range couplings, J. Phys. Commun. **2**, 045010 (2018).

[17] F. Ares, J. G. Esteve, F. Falceto, and A. R. de Queiroz, Entanglement entropy in the long-range Kitaev chain, Phys. Rev. A **97**, 062301 (2018).

[18] D. T. Liu, J. Shabani, and A. Mitra, Long-range Kitaev chains via planar Josephson junctions, Phys. Rev. B **97**, 235114 (2018).

[19] U. Bhattacharya and A. Dutta, Topological footprints of the Kitaev chain with long-range superconducting pairings at a finite temperature, Phys. Rev. B **97**, 214505 (2018).

[20] S. Lieu, D. K. K. Lee, and J. Knolle, Disorder protected and induced local zero-modes in longer-range Kitaev chains, Phys. Rev. B **98**, 134507 (2018).

[21] U. Bhattacharya, S. Maity, A. Dutta, and D. Sen, Critical phase boundaries of static and periodically kicked long-range Kitaev chain, J. Phys.: Condens. Matter **31**, 174003 (2019).

[22] R. Nehra, A. Sharma, and A. Soori, Transport in a long-range Kitaev ladder: Role of Majorana and subgap Andreev states, Europhys. Lett. **130**, 27003 (2020).

[23] U. Mishra, R. Jafari, and A. Akbari, Disordered Kitaev chain with long-range pairing: Loschmidt echo revivals and dynamical phase transitions, J. Phys. A: Math. Theor. **53**, 375301 (2020).

[24] Z. Tao, T. Yan, W. Liu, J. Niu, Y. Zhou, L. Zhang, H. Jia, W. Chen, S. Liu, Y. Chen, and D. Yu, Simulation of a topological phase transition in a Kitaev chain with long-range coupling using a superconducting circuit, Phys. Rev. B **101**, 035109 (2020).

[25] D. Giuliano, S. Paganelli, and L. Lepori, Current transport properties and phase diagram of a Kitaev chain with long-range pairing, Phys. Rev. B **97**, 155113 (2018).

[26] S. Tewari, J. D. Sau, and S. Das Sarma, A theorem for the existence of Majorana fermion modes in spin-orbit-coupled semiconductors, Ann. Phys. **325**, 219 (2010).

[27] J. D. Sau, R. M. Lutchyn, S. Tewari, and S. Das Sarma, Generic New Platform for Topological Quantum Computation using

Semiconductor Heterostructures, Phys. Rev. Lett. **104**, 040502 (2010).

[28] R. M. Lutchyn, J. D. Sau, and S. Das Sarma, Majorana Fermions and a Topological Phase Transition in Semiconductor-Superconductor Heterostructures, Phys. Rev. Lett. **105**, 077001 (2010).

[29] Y. Oreg, G. Refael, and F. von Oppen, Helical Liquids and Majorana Bound States in Quantum Wires, Phys. Rev. Lett. **105**, 177002 (2010).

[30] J. Alicea, Majorana fermions in a tunable semiconductor device, Phys. Rev. B **81**, 125318 (2010).

[31] J. D. Sau, S. Tewari, R. M. Lutchyn, T. D. Stanescu, and S. Das Sarma, Non-Abelian quantum order in spin-orbit-coupled semiconductors: Search for topological Majorana particles in solid-state systems, Phys. Rev. B **82**, 214509 (2010).

[32] T. D. Stanescu, R. M. Lutchyn, and S. Das Sarma, Majorana fermions in semiconductor nanowires, Phys. Rev. B **84**, 144522 (2011).

[33] J. Alicea, Y. Oreg, G. Refael, F. von Oppen, and M. P. A. Fisher, Non-Abelian statistics and topological quantum information processing in 1D wire networks, Nat. Phys. **7**, 412 (2011).

[34] V. Mourik, K. Zuo, S. M. Frolov, S. R. Plissard, E. P. A. M. Bakkers, and L. P. Kouwenhoven, Signatures of Majorana fermions in hybrid superconductor-semiconductor nanowire devices, Science **336**, 1003 (2012).

[35] A. Das, Y. Ronen, Y. Most, Y. Oreg, M. Heiblum, and H. Shtrikman, Zero-bias peaks and splitting in an Al-InAs nanowire topological superconductor as a signature of Majorana fermions, Nat. Phys. **8**, 887 (2012).

[36] M. T. Deng, C. L. Yu, G. Y. Huang, M. Larsson, P. Caroff, and H. Q. Xu, Anomalous zero-bias conductance peak in a Nb-InSb nanowire-Nb hybrid device, Nano Lett. **12**, 6414 (2012).

[37] H. O. H. Churchill, V. Fatemi, K. Grove-Rasmussen, M. T. Deng, P. Caroff, H. Q. Xu, and C. M. Marcus, Superconductor-nanowire devices from tunneling to the multichannel regime: Zero-bias oscillations and magnetoconductance crossover, Phys. Rev. B **87**, 241401(R) (2013).

[38] A. D. K. Finck, D. J. Van Harlingen, P. K. Mohseni, K. Jung, and X. Li, Anomalous Modulation of a Zero-Bias Peak in a Hybrid Nanowire-Superconductor Device, Phys. Rev. Lett. **110**, 126406 (2013).

[39] F. Nichele, A. C. C. Drachmann, A. M. Whiticar, E. C. T. O'Farrell, H. J. Suominen, A. Fornieri, T. Wang, G. C. Gardner, C. Thomas, A. T. Hatke, P. Krogstrup, M. J. Manfra, K. Flensberg, and C. M. Marcus, Scaling of Majorana Zero-Bias Conductance Peaks, Phys. Rev. Lett. **119**, 136803 (2017).

[40] S. M. Albrecht, A. P. Higginbotham, M. Madsen, F. Kuemmeth, T. S. Jespersen, J. Nyg, P. Krogstrup, and C. M. Marcus, Exponential protection of zero modes in Majorana islands, Nature (London) **531**, 206 (2016).

[41] H. Zhang, C.-X. Liu, S. Gazibegovic, D. Xu, J. A. Logan, G. Wang, N. van Loo, J. D. S. Bommer, M. W. A. de Moor, D. Car, R. L. M. Op het Veld, P. J. van Veldhoven, S. Koelling, M. A. Verheijen, M. Pendharkar, D. J. Pennachio, B. Shojaei, J. S. Lee, C. J. Palmstrøm, E. P. A. M. Bakkers *et al.*, Quantized Majorana conductance, Nature (London) **556**, 74 (2018).

[42] G. Kells, D. Meidan, and P. W. Brouwer, Near-zero-energy end states in topologically trivial spin-orbit coupled superconducting nanowires with a smooth confinement, Phys. Rev. B **86**, 100503(R) (2012).

[43] J. Liu, A. C. Potter, K. T. Law, and P. A. Lee, Zero-Bias Peaks in the Tunneling Conductance of Spin-Orbit-Coupled Superconducting Wires with and without Majorana End-States, Phys. Rev. Lett. **109**, 267002 (2012).

[44] D. Chevallier, D. Sticlet, P. Simon, and C. Bena, Mutation of Andreev into Majorana bound states in long superconductor-normal and superconductor-normal-superconductor junctions, Phys. Rev. B **85**, 235307 (2012).

[45] D. Roy, N. Bondyopadhaya, and S. Tewari, Topologically trivial zero-bias conductance peak in semiconductor Majorana wires from boundary effects, Phys. Rev. B **88**, 020502(R) (2013).

[46] H. J. Suominen, M. Kjaergaard, A. R. Hamilton, J. Shabani, C. J. Palmstrøm, C. M. Marcus, and F. Nichele, Zero-Energy Modes from Coalescing Andreev States in a Two-Dimensional Semiconductor-Superconductor Hybrid Platform, Phys. Rev. Lett. **119**, 176805 (2017).

[47] C. Moore, T. D. Stanescu, and S. Tewari, Two-terminal charge tunneling: Disentangling Majorana zero modes from partially separated Andreev bound states in semiconductor-superconductor heterostructures, Phys. Rev. B **97**, 165302 (2018).

[48] C. Moore, C. Zeng, T. D. Stanescu, and S. Tewari, Quantized zero-bias conductance plateau in semiconductor-superconductor heterostructures without topological Majorana zero modes, Phys. Rev. B **98**, 155314 (2018).

[49] J. Manousakis, C. Wille, A. Altland, R. Egger, K. Flensberg, and F. Hassler, Weak Measurement Protocols for Majorana Bound State Identification, Phys. Rev. Lett. **124**, 096801 (2020).

[50] H.-Z. Lu, Using noise to detect Majorana states, Physics **13**, 30 (2020).

[51] W. DeGottardi, M. Thakurathi, S. Vishveshwara, and D. Sen, Majorana fermions in superconducting wires: Effects of long-range hopping, broken time-reversal symmetry, and potential landscapes, Phys. Rev. B **88**, 165111 (2013).

[52] M. Kompaniiets, O. V. Dobrovolskiy, C. Neetzel, F. Porrati, J. Brötz, W. Ensinger, and M. Huth, Long-range superconducting proximity effect in polycrystalline Co nanowires, Appl. Phys. Lett. **104**, 052603 (2014).

[53] H. Wang, L. B. Shao, Y. X. Zhao, L. Sheng, B. G. Wang, and D. Y. Xing, Effective long-range pairing and hopping in topological nanowires weakly coupled to *s*-wave superconductors, Phys. Rev. B **98**, 174512 (2018).

[54] B. Bhattacharyya, V. P. S. Awana, T. D. Senguttuvan, V. N. Ojha, and S. Husale, Proximity-induced supercurrent through topological insulator based nanowires for quantum computation studies, Sci. Rep. **8**, 17237 (2018).

[55] Y. Lu and T. T. Heikkilä, Proximity effect in superconducting heterostructures with strong spin-orbit coupling and spin splitting, Phys. Rev. B **100**, 104514 (2019).

[56] R.-X. Zhang and C.-X. Liu, Crystalline Symmetry-Protected Majorana Mode in Number-Conserving Dirac Semimetal Nanowires, Phys. Rev. Lett. **120**, 156802 (2018).

[57] M. F. Lapa and M. Levin, Rigorous Results on Topological Superconductivity with Particle Number Conservation, Phys. Rev. Lett. **124**, 257002 (2020).

[58] E. M. Stoudenmire, J. Alicea, O. A. Starykh, and M. P. A. Fisher, Interaction effects in topological superconducting wires supporting Majorana fermions, Phys. Rev. B **84**, 014503 (2011).

[59] F. Pientka, L. I. Glazman, and F. von Oppen, Topological superconducting phase in helical Shiba chains, Phys. Rev. B **88**, 155420 (2013).

[60] F. Pientka, L. I. Glazman, and F. von Oppen, Unconventional topological phase transitions in helical Shiba chains, Phys. Rev. B **89**, 180505(R) (2014).

[61] C.-K. Chiu, J. C. Y. Teo, A. P. Schnyder, and S. Ryu, Classification of topological quantum matter with symmetries, Rev. Mod. Phys. **88**, 035005 (2016).

[62] A. P. Schnyder, S. Ryu, A. Furusaki, and A. W. W. Ludwig, Classification of topological insulators and superconductors in three spatial dimensions, Phys. Rev. B **78**, 195125 (2008).

[63] S. Maity, U. Bhattacharya, and A. Dutta, One-dimensional quantum many body systems with long-range interactions, J. Phys. A: Math. Theor. **53**, 013001 (2019).

[64] H.-F. Lü, H.-Z. Lu, and S.-Q. Shen, Nonlocal noise cross correlation mediated by entangled Majorana fermions, Phys. Rev. B **86**, 075318 (2012).

[65] T. Jonckheere, J. Rech, A. Zazunov, R. Egger, A. L. Yeyati, and T. Martin, Giant Shot Noise from Majorana Zero Modes in Topological Trijunctions, Phys. Rev. Lett. **122**, 097003 (2019).

[66] H.-F. Lü, H.-Z. Lu, and S.-Q. Shen, Current noise cross correlation mediated by Majorana bound states, Phys. Rev. B **90**, 195404 (2014).

[67] H.-F. Lü, H.-Z. Lu, and S.-Q. Shen, Enhanced current noise correlations in a Coulomb-Majorana device, Phys. Rev. B **93**, 245418 (2016).

[68] A. Golub and B. Horovitz, Shot noise in a Majorana fermion chain, Phys. Rev. B **83**, 153415 (2011).

[69] L. Tosi, C. Metzger, M. F. Goffman, C. Urbina, H. Pothier, S. Park, A. L. Yeyati, J. Nygård, and P. Krogstrup, Spin-Orbit Splitting of Andreev States Revealed by Microwave Spectroscopy, Phys. Rev. X **9**, 011010 (2019).

[70] G. C. Ménard, G. L. R. Anselmetti, E. A. Martinez, D. Puglia, F. K. Malinowski, J. S. Lee, S. Choi, M. Pendharkar, C. J. Palmstrøm, K. Flensberg, C. M. Marcus, L. Casparis, and A. P. Higginbotham, Conductance-Matrix Symmetries of a Three-Terminal Hybrid Device, Phys. Rev. Lett. **124**, 036802 (2020).